

Data-driven model comparing the effects of glial scarring and interface interactions on chronic neural recordings in non-human primates

This content has been downloaded from IOPscience. Please scroll down to see the full text.

2016 J. Neural Eng. 13 016010

(<http://iopscience.iop.org/1741-2552/13/1/016010>)

View [the table of contents for this issue](#), or go to the [journal homepage](#) for more

Download details:

IP Address: 141.212.148.10

This content was downloaded on 14/12/2015 at 16:49

Please note that [terms and conditions apply](#).

Data-driven model comparing the effects of glial scarring and interface interactions on chronic neural recordings in non-human primates

Karlo A Malaga¹, Karen E Schroeder¹, Paras R Patel¹, Zachary T Irwin¹, David E Thompson¹, J Nicole Bentley², Scott F Lempka³, Cynthia A Chestek^{1,4} and Parag G Patil^{1,2,4}

¹ Department of Biomedical Engineering, University of Michigan, Ann Arbor, MI, USA

² Department of Neurosurgery, University of Michigan Health System, Ann Arbor, MI, USA

³ Center for Neurological Restoration, Cleveland Clinic Foundation, Cleveland, OH, USA

E-mail: cchestek@umich.edu and pgpatil@med.umich.edu

Received 10 June 2015, revised 4 October 2015

Accepted for publication 26 October 2015

Published 14 December 2015



CrossMark

Abstract

Objective. We characterized electrode stability over twelve weeks of impedance and neural recording data from four chronically-implanted Utah arrays in two rhesus macaques, and investigated the effects of glial scarring and interface interactions at the electrode recording site on signal quality using a computational model. **Approach.** A finite-element model of a Utah array microelectrode in neural tissue was coupled with a multi-compartmental model of a neuron to quantify the effects of encapsulation thickness, encapsulation resistivity, and interface resistivity on electrode impedance and waveform amplitude. The coupled model was then reconciled with the *in vivo* data. Histology was obtained seventeen weeks post-implantation to measure gliosis. **Main results.** From week 1–3, mean impedance and amplitude increased at rates of 115.8 k Ω /week and 23.1 μ V/week, respectively. This initial ramp up in impedance and amplitude was observed across all arrays, and is consistent with biofouling (increasing interface resistivity) and edema clearing (increasing tissue resistivity), respectively, in the model. Beyond week 3, the trends leveled out. Histology showed that thin scars formed around the electrodes. In the model, scarring could not match the *in vivo* data. However, a thin interface layer at the electrode tip could. Despite having a large effect on impedance, interface resistivity did not have a noticeable effect on amplitude. **Significance.** This study suggests that scarring does not cause an electrical problem with regard to signal quality since it does not appear to be the main contributor to increasing impedance or significantly affect amplitude unless it displaces neurons. This, in turn, suggests that neural signals can be obtained reliably despite scarring as long as the recording site has sufficiently low impedance after accumulating a thin layer of biofouling. Therefore, advancements in microelectrode technology may be expedited by focusing on improvements to the recording site-tissue interface rather than elimination of the glial scar.

 Online supplementary data available from stacks.iop.org/JNE/13/016010/mmedia

Keywords: neural recording, computational model, brain-machine interface

(Some figures may appear in colour only in the online journal)

⁴ Contributed equally to the work.

1. Introduction

A brain–machine interface (BMI) is a type of neuroprosthetic device aimed towards restoring lost motor, sensory, and/or cognitive function to patients with neurological disorders [1–3]. BMIs use electrical signals from the brain to control external devices such as computer cursors, robotic limbs, and exoskeletons. These neural signals can come from various sources such as electroencephalography, electrocorticography, and single-unit recordings, which differ in their degree of invasiveness, amplitude, and bandwidth. For single-unit recordings, action potentials from individual neurons are measured using electrodes implanted in the brain. Notable examples of intracortical microelectrode arrays used to record single-unit activity include microwires [4], Michigan probes [5], and Utah arrays [6]. Recordings from such devices provide high spatial resolution. However, it can be difficult to identify and isolate individual units. For BMIs to become clinically viable, electrode arrays must be able to acquire stable, high-quality signals for years. Currently, the ability to reliably record single-unit activity with intracortical microelectrode arrays is hindered by low signal-to-noise ratio (SNR). A low SNR can come from a variety of biological, material, or mechanical failure modes [7].

Over time, signal quality can be affected by many different factors. One factor is the brain tissue response [8–11], which occurs when electrodes are implanted in the brain. This response is divided into two phases: (1) an acute inflammatory response and (2) a chronic foreign body reaction. The acute phase starts upon electrode insertion, is characterized by edema and activated microglia, and usually lasts 1–3 weeks. The chronic phase starts after the acute tissue reaction subsides and is characterized by the formation of a fibrous encapsulation layer around the electrodes, termed glial scarring/encapsulation and/or gliosis, by reactive astrocytes. This accumulation of cells surrounds the surface of the electrodes and is usually complete within 6–8 weeks. The glial scar is hypothesized to decrease signal quality [12–15]. However, there is no accepted electrical explanation for how this occurs. Possible explanations include increased impedance due to the scar insulating the electrode [12, 13, 16, 17] and isolation of the electrode from nearby neurons in the surrounding tissue due to growth of the encapsulation layer (i.e., decreased neuronal density) [14, 15]. The mechanisms underlying glial scar formation have been studied extensively. However, a consensus regarding its effect on chronic neural recordings has yet to be determined. Some studies have reported conflicting results, showing variable signal quality during the scar formation period followed by still-identifiable neural signals over subsequent months [7, 18–22]. Furthermore, it is unclear if the glial scar is responsible for device failure multiple years after implantation.

Although less studied, material degradation is another major failure mechanism of implantable electrode arrays [7]. To enhance biocompatibility and facilitate recording, electrodes are coated with an insulating material (e.g., polyimide, Parylene C) and metal (e.g., platinum, iridium oxide) is applied to the recording site, respectively. Over time, these

materials may start to degrade [23–25]. For example, the electrode insulation could develop cracks [23, 24] or the tip metallization could be lost [25]. Therefore, many groups have started investigating alternative coating techniques and materials to extend device longevity [26–30]. Material failures have become more of a concern with regard to signal stability over time since the glial scar may stabilize within a few months [7].

Another factor that is hypothesized to impact signal quality is the adsorption of proteins on the recording site, termed biofouling. Since biofouling may increase electrode impedance, efforts have been made to reduce the extent of it [29, 30]. One approach is to coat the electrode with anti-fouling materials before implantation. For example, coating with polyethylene glycol has been found to reduce protein adsorption and prevent impedance increases [29, 30].

Alongside experimental studies, there have been a number of computational models developed to better understand neural recordings and how they are affected by different factors [31–35]. Such models are useful for performing analyses that would be difficult to implement experimentally and continue to grow in complexity. For example, they have included explicit representation of a microelectrode implanted in the brain, populated the surrounding tissue with hundreds of individual neuron models, and incorporated sources of thermal and biological noise [33, 34]. Results from these models have been consistent with and validated by experimental findings [36]. They can also make interesting predictions that can influence and encourage further investigation. For example, one modeling study predicted that electrode encapsulation results in increased waveform amplitude [33], which conflicts with current assumptions regarding the effect of the glial scar on single-unit recordings.

In this study, we characterized electrode stability over twelve weeks of impedance (1 kHz) and broadband ($f_s = 30$ kHz) neural recording data from four chronically-implanted Utah arrays in two rhesus macaques (two arrays/monkey). We then investigated the effect of the glial scar, also known as glial encapsulation and/or gliosis, and interface between the recording site and surrounding neural tissue on signal quality using a data-driven neural recording model. A previously-described computational model [33, 34] was modified with the specific geometry and material properties of a Utah array microelectrode to quantify the effect of encapsulation thickness, encapsulation resistivity, and interface resistivity on electrode impedance and waveform amplitude. The model was then reconciled with the *in vivo* data. Histology, stained for microglia, was obtained from one monkey seventeen weeks post-implantation to measure gliosis around the electrodes.

2. Methods

2.1. Experimental methods

2.1.1. Data acquisition. All procedures were carried out in accordance with protocols approved by the University

Committee on Use and Care of Animals at the University of Michigan. Two rhesus macaques were each implanted with two Utah arrays (Blackrock Microsystems, Salt Lake City, UT, USA) in finger and hand areas of primary motor cortex (M1) using standard neurosurgical techniques [37]. The arrays had 96 active electrode channels, platinum [$\sim 400\text{ k}\Omega$ (1 kHz)] electrode site metal, and parylene C insulation. The target region was located by identifying the point where the spur of the arcuate sulcus would intersect the central sulcus. The arrays were then placed at this location, just anterior to the central sulcus.

The two monkeys were trained to sit quietly in a chair (Crist Instrument Co., Inc., Hagerstown, MD, USA) during recording sessions, which consisted of two minutes of calm sitting. Broadband neural data were sampled at 30 kHz and recorded using a Cerebus neural signal processor (Blackrock Microsystems). Multi-unit recordings were obtained by thresholding at $-4.5x$ the rms noise on each electrode. After each session, 1 kHz impedance measurements were obtained from each electrode using the same Cerebus system starting one week post-implantation. Complex impedance measurements were also obtained from seven electrodes from one array using a precision LCR meter (LCR-8110G) (GW Instek, New Taipei City, Taiwan). Measurements were taken 2.5 weeks post-implantation at fourteen equally spaced (150 Hz) frequencies between 100 and 2050 Hz using a two-electrode setup, with one electrode on the measured pin and the other on the ground pin. Histology was obtained from one monkey after it was euthanized due to an unrelated health concern. This occurred after the conclusion of this study.

2.1.2. Data analysis. From four arrays in two monkeys (two arrays/monkey), *in vivo* data from the first twelve weeks post-implantation were analyzed offline. The first twelve weeks were chosen since this is the critical period of scar formation [11]. Electrodes were excluded from further analyses if any of their weekly impedance measurements (12 measurements/electrode) exceeded $2.5\text{ M}\Omega$. This was done since such high impedances often come from damaged electrodes [25]. Of the 384 total electrodes (4 arrays \times 96 electrodes/array), 96 were excluded across all four arrays. Specifically, 1, 26, 46, and 23 electrode(s) had a least one impedance measurement greater than $2.5\text{ M}\Omega$ from array S-1, S-2, K-1, and K-2, respectively (supplementary data). In addition to looking at all viable ($Z < 2.5\text{ M}\Omega$) electrodes ($n = 288$), the top twenty electrodes ($n = 80$) with the largest single-units from each array were analyzed separately. Multiple comparisons for one-way analysis of variance were used to compare mean electrode impedance (1 kHz) and waveform amplitude (peak-to-peak) between different weeks. False discovery rate control and bootstrapping were used to identify significant trends for individual electrodes. All analyses were performed in MATLAB (The MathWorks, Inc., Natick, MA, USA).

2.1.3. Histology. Histology, stained for microglia, was obtained from one monkey seventeen weeks post-

implantation to measure gliosis around the electrodes. Tissue sections were taken from one array along the shanks, where the glial scar is likely larger compared to at the tips [38]. The section was first soaked in 4% (w/v) paraformaldehyde (P6148) (Sigma-Aldrich, St. Louis, MO, USA) in 1x phosphate buffered saline (PBS) (BP3994) (Fisher Scientific, Waltham, MA, USA) for 24 h. Once fixed, the tissue was cryoprotected by successive 24 h long soaks in 10%, 20%, and 30% (w/v) D-Sucrose (BP220) (Fisher Scientific) in 1x PBS. The tissue was then embedded in Tissue-Tek O.C.T. Compound (4583) (Sakura Finetek Europe B.V., Alphen aan den Rijn, The Netherlands) and frozen at -20°C . The frozen sample was sectioned into $20\text{ }\mu\text{m}$ thick slices using a Microm HM550 cryostat (Fisher Scientific) and mounted directly onto slides. A hydrophobic barrier was then drawn around each slice using an ImmEdge pen (22312) (Ted Pella, Inc., Redding, CA, USA) and allowed to dry.

Before staining, the slices were rinsed with 1x PBS for 10 min. They were then blocked with 10% normal goat serum blocking solution (S-1000) (Vector Laboratories, Inc., Burlingame, CA, USA) in 1x PBS for 1 h at room temperature and incubated in a solution of Anti Iba1, Rabbit (1:1000 dilution) (019-19741) (Wako Chemicals USA, Inc., Richmond, VA, USA), 0.3% Triton X-100 (T8787) (Sigma-Aldrich), and 3% normal goat serum blocking solution in 1x PBS overnight in a covered chamber. The following day, the slices were triple rinsed with 1x PBS, with each rinse sitting for 10 min. They were then incubated in a solution of Goat anti-Rabbit IgG (H + L) Secondary Antibody, Alexa Fluor 546 conjugate (1:200 dilution) (A-11035) (Life Technologies, Grand Island, NY, USA), 0.2% Triton X-100, and 5% normal goat serum blocking solution in 1x PBS for 2 h at room temperature. Next, the slices were double rinsed with 1x PBS, with each rinse lasting 10 min. Slides were then coverslipped using ProLong Gold Antifade Mountant (P36930) (Life Technologies) and allowed to dry overnight before imaging. A LSM 510 META Laser Scanning Confocal Microscope (Zeiss, Oberkochen, Germany) was used to image the stained slices. Encapsulation thickness was estimated by taking clockwise (3, 6, 9, and 12 o'clock) measurements of the glial scar around the electrodes and averaging the values.

2.2. Computational methods

2.2.1. Finite-element model (FEM). The neural recording model used in this study was similar to previously-described computational models [31, 33, 34]. The model consisted of two main components: (1) a three-dimensional FEM of a microelectrode implanted in neural tissue and (2) a multi-compartmental model of a neuron. The FEM was assumed to be electrostatic since the impedance of gray matter is relatively frequency-independent [39]. The FEM was generated and solved in COMSOL Multiphysics 4.4 (COMSOL, Inc., Burlington, MA, USA), as shown in figures 1(a) and (b). The surrounding tissue was modeled as a cylinder with a height of $16\text{ }000\text{ }\mu\text{m}$ and radius of $8\text{ }000\text{ }\mu\text{m}$, while the electrode was modeled as a Utah array microelectrode [6]. The electrode consisted of: (1) a conical

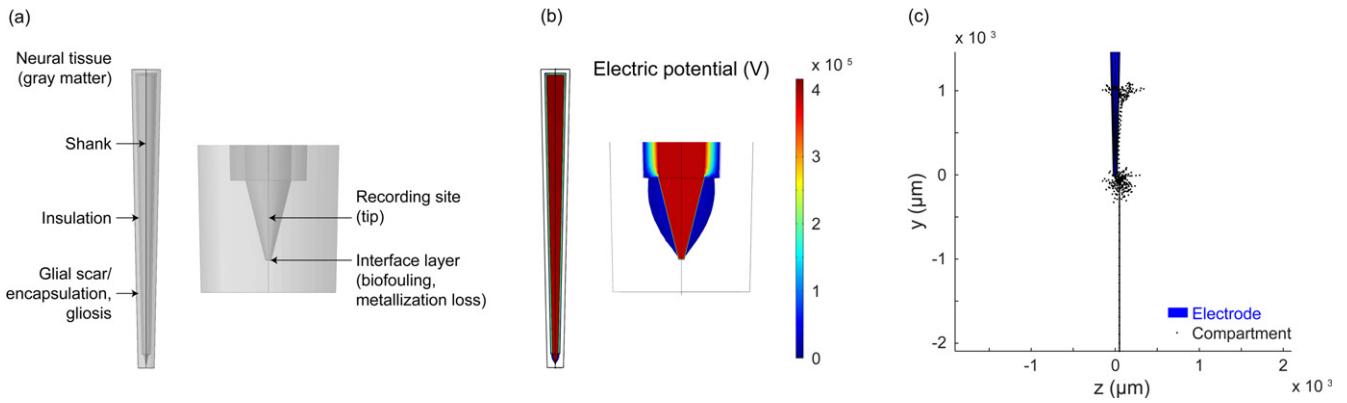


Figure 1. Neural recording model. (a) FEM geometry and domains. The glial scar/encapsulation, gliosis domain corresponds to the layer surrounding the entire electrode. The interface layer (biofouling, metallization loss) domain corresponds to the thin layer surrounding the electrode tip. (b) FEM solution. (c) Compartmental model. The axon is parallel to the electrode and the soma is 50 μm away from the bottom of the tip.

Table 1. Material and electrical resistivity of FEM domains.

Domain	Material	Electrical resistivity ($\Omega\text{ cm}$)
Shank	Doped silicon	3.3
Recording site (tip)	Platinum	1.1×10^{-5}
Insulation	Parylene C	1×10^{15} [25]
Glial scar/encapsulation, gliosis	n/a	600 [43]
Interface layer (biofouling, metallization loss)	n/a	1.8×10^5
Neural tissue (gray matter)	n/a	300 [44]

shank with a height of 1450 μm , top radius of 45 μm , and bottom radius of 14 μm , (2) a conical tip with a height of 50 μm , top radius of 14 μm , and bottom radius of 1.5 μm (exposed surface area = 2517 μm^2), and (3) an insulation layer around the shank with a uniform thickness of 10 μm . The microelectrode was placed at the center of the neural tissue, such that the center of the bottom of the shank/top of the tip was at the origin. The tip was surrounded by a thin layer with a uniform thickness of 0.5 μm to incorporate the interface between the recording site and surrounding tissue into the FEM [40–42]. In reality, this interface layer has a thickness on the order of nanometers [42], and, ideally, it would be represented to scale in the FEM. However, meshing such a thin layer of finite thickness requires a large computational cost. To work around this constraint, the interface layer was made thicker and its electrical properties were adapted to account for the increase in thickness [42]. This was the trade-off between having a realistic model and one that was computationally efficient without reducing accuracy. To complete the FEM, the electrode, including the interface, was surrounded by a layer with a uniform thickness of 20 μm to incorporate the glial scar. The default thickness of the scar was estimated from histology (described below) and was comparable to other observed encapsulation thicknesses [9, 10].

The material and electrical resistivity of the FEM domains are shown in table 1. Each domain had a uniform resistivity, which was either acquired or derived from the literature. The interface layer resistivity was estimated with

complex impedance data from seven viable electrodes from one array (described above). A previously-described equivalent circuit model for the electrode–tissue interface was used to isolate the interface component [12, 13, 16, 34]. Briefly, the interface can be modeled as a constant phase element (CPE). CPE impedance (Z_{CPE}) was calculated using the following equation:

$$Z_{\text{CPE}} = \frac{K}{(j\omega)^\alpha},$$

where K is an electrode impedance scaling factor, j is the imaginary number, ω is the angular frequency, and α is a phase term defined over $0 \leq \alpha \leq 1$. K [$1.9 \times 10^7 \Omega\text{ s}^{-\alpha}$ (1 kHz)] and α (0.5) were estimated by fitting the impedance data to the equivalent circuit model and used to calculate Z_{CPE} . The magnitude of Z_{CPE} ($|Z_{\text{CPE}}|$) was taken to account for the resistive and capacitive components of the impedance. Since the FEM was assumed to be electrostatic and recording electrodes are typically characterized with impedance measurements at 1 kHz, $|Z_{\text{CPE}}|$ was only calculated at that frequency [353.7 k Ω (1 kHz)] [42]. In the FEM, the interface layer resistivity ($1.8 \times 10^5 \Omega\text{ cm}$) that yielded an interface impedance (369.3 k Ω) closest to the calculated $|Z_{\text{CPE}}|$ was chosen as the default parameter value.

The FEM was meshed, with finer meshing applied at the electrode and its layers, and consisted of 685 049 elements. To test for model convergence, the mesh density of the FEM was increased. Increasing the number of elements by 3.5x resulted in a 0.01% change (+0.04 k Ω) in the value of the

total system impedance. Therefore, the initial mesh density used was sufficient to confirm model convergence and ensure solution accuracy. The default mesh was used for all simulations involving changes in encapsulation and interface resistivity. Only the resistivity parameter values were adjusted (one at a time) before solving the FEM again (i.e., the FEM was not remeshed). For simulations involving changes in encapsulation thickness, the FEM had to be remeshed for each condition before a solution could be obtained. However, the mesh settings were not changed between simulations. To solve for the electric potential distribution, a load and boundary condition was defined. The load condition was a 1 A point current source placed at the bottom of the tip (described below). This current source was applied at a single element located in the center of the tip domain boundary. The boundary condition required that the surface of the surrounding neural tissue be set to ground. Electrode impedance was calculated by measuring the voltage drop from the bottom of the tip to ground after solving the FEM and dividing by the current source (1 A).

2.2.2. Multi-compartmental model. The compartmental model, as shown in figure 1(c), was a layer V pyramidal cell from cat visual cortex that generated action potentials via excitatory synaptic inputs at the apical dendrites [31, 33, 34]. Simulations were performed in NEURON 7.3 [45] to solve for the transmembrane currents generated in each compartment ($n = 531$) of the neuron during an action potential.

2.2.3. Model coupling. The FEM and compartmental model were coupled in MATLAB to complete the computational model. This was accomplished by loading the electric potential distribution solved in COMSOL and the compartment coordinates and currents calculated in NEURON into MATLAB. In the coupled FEM-compartmental model, each neuron compartment was represented as a point current source and was placed accordingly within the FEM. The neuron model was rotated such that the axon was parallel to the electrode and translated such that the soma was 50 μm away from the bottom of the tip (figure 1(c)). Unless otherwise noted, the simulated action potential recorded at the tip was calculated using previously-described methods [33, 34]. Briefly, the potential (Φ) was calculated using the following equation:

$$\Phi = KJ,$$

where K is a $(1 \times n)$ vector of the potentials that would be generated at the tip due to each of the n compartment currents and J is a $(n \times t)$ matrix of the compartment currents at each of the t time steps. The J matrix was calculated in NEURON and the K vector was derived from the FEM using a reciprocal solution. This involved applying a unit point current source (1 A) at a single element located in the center of the bottom boundary of the tip domain and then solving for the electric potential distribution in COMSOL. By the theorem of reciprocity, the potential induced at any given element within the FEM by the unit point current source applied at the

electrode tip can be considered to be the potential that would be induced at the tip by a unit point current source applied at the same element [33, 34]. For example, if a 1 V potential at element n is induced by the 1 A current source applied at the electrode tip, then the theorem of reciprocity stipulates that a 1 A current source applied at element n will induce a 1 V potential at the tip. Therefore, the potential recorded at the electrode tip can be calculated by summing the individual contributions from each compartment current of the neuron model. Since the spatial location of the compartments within the FEM did not necessarily correspond to an element of the mesh, the potentials induced by each point current source had to be interpolated from the elements nearest each compartment in MATLAB.

3. Results

3.1. Electrode impedance

Many existing hypotheses regarding device failure in chronic neural recordings involve increasing amounts of reactive tissue around the electrodes over time, which may increase electrode impedance [12, 13, 16, 17]. Therefore, impedance was examined over the first twelve weeks post-implantation to determine if it increased. 1 kHz impedance measurements were collected from the four arrays. One array was later excluded from the pooled array analyses since it pulled out of the brain due to tension on the wire. However, its individual analyses are included in the supplementary data. Of the 288 viable electrodes, 50 were excluded from this array. Figure 2(a) shows mean impedance (821.8 k Ω overall) for all viable electrodes from three arrays ($n = 238$). An overall linear increase of 12.2 k Ω /week was observed, but it was not significant ($p = 0.09$) at the 0.05 level. Characteristic of Utah arrays, a subset of electrodes had large, well-defined single-units, while most of the others had smaller single- or multi-units. Therefore, impedance (785.3 k Ω overall) was also examined for the top twenty electrodes with the largest single-units from three arrays ($n = 60$). An overall linear increase of 12.8 k Ω /week was observed, but it also was not significant ($p = 0.06$) at the 0.05 level.

Lack of a significant overall linear increase does not preclude a more resistive medium developing around the electrodes. The initial ramp in impedance during the first three weeks post-implantation [115.8 k Ω /week ($p = 0.04$, all viable), 99.9 k Ω /week ($p = 0.21$, top twenty)] stands out and is nominally consistent with scarring onset [8–11] and bio-fouling [29, 30]. Beyond week 3, the trend leveled out [−0.7 k Ω /week ($p = 0.91$, all viable), 4.2 k Ω /week ($p = 0.60$, top twenty)]. Figure 2(b) shows mean impedance at week 1, 2, 3, and 12. Week 3 was significantly different from week 1 ($p < 0.001$, multiple comparisons). However, there was no significant difference between week 3 and week 2 and 12 ($p > 0.05$, multiple comparisons).

To determine if this impedance trend was consistent with a previously-described tissue encapsulation model [33, 34], a sensitivity analysis of encapsulation thickness was performed

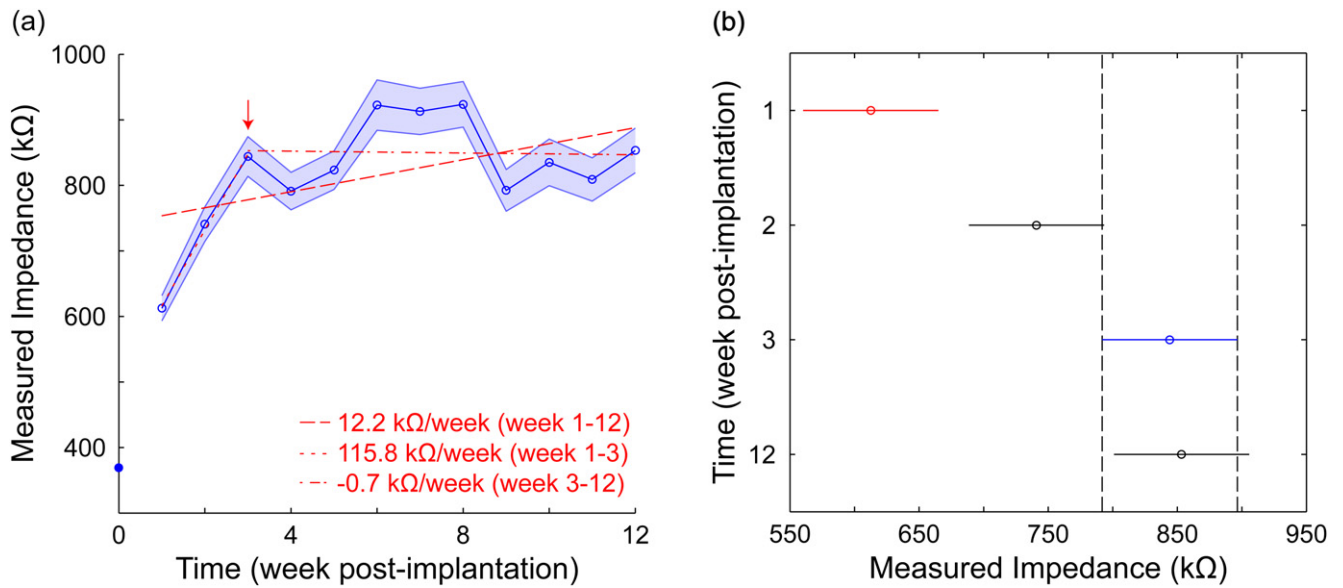


Figure 2. Mean impedance (1 kHz) over time (pooled arrays (3/4), all viable electrodes). (a) Week 1–12. Red lines are the linear regression fits. Arrow denotes week 3. Solid circle denotes the mean pre-implantation impedance. Error bars denote the standard error of the mean. (b) Week 1, 2, 3, and 12. Bars denote the comparison intervals. Colour denotes the test group (blue) and significantly different groups (red).

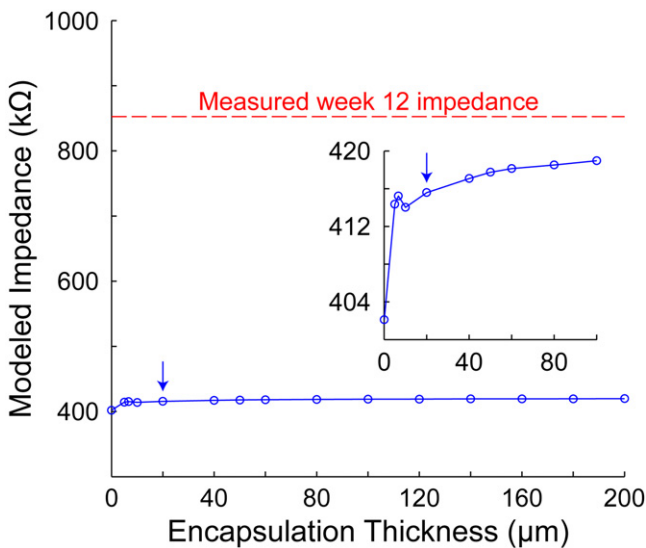


Figure 3. Effect of encapsulation thickness on impedance. Arrow denotes the default encapsulation thickness (20 μm). Inset expands the first half of the data.

in a modified version of said model, which included the specific geometry and material properties of a Utah array microelectrode. With a default encapsulation and interface resistivity of 600 and $1.8 \times 10^5 \Omega \text{ cm}$, respectively, encapsulation thickness had a small effect on impedance, as shown in figure 3. For example, a 10x increase (20 to 200 μm) in encapsulation thickness resulted in a mere 1.0% increase (+4.1 k Ω) in impedance. This makes sense since impedance is inversely proportional to the cross-sectional area of the electrode plus the encapsulation layer. As the encapsulation layer thickens, the total cross-sectional area increases. Therefore, any increase in impedance due to the scar thickening is offset by the accompanying increase in total cross-

sectional area. Furthermore, there were no significant differences in impedance between simulations with and without an encapsulation layer (i.e., encapsulation resistivity = neural tissue resistivity = 300 $\Omega \text{ cm}$). For example, increasing encapsulation thickness from 0 to 5 μm resulted in only a 3.0% increase (+12.3 k Ω) in impedance and increasing it further had diminishing returns due to increasing cross-sectional area, as previously stated. Therefore, the model was unable to adequately match the observed changes in impedance when it only considered the glial scar. This suggests that scarring is not the main contributor to increasing impedance, assuming that the scar is not dramatically more resistive than the surrounding neural tissue (described below).

Histology also confirmed that the contiguous scars did not thicken significantly. Instead, relatively thin scars formed around the electrodes. Figure 4 shows histology, stained for microglia, obtained from one monkey seventeen weeks post-implantation. Mean microglial encapsulation thickness was 16.1 μm with a standard deviation of 10.0 μm , comparable to other observed encapsulation thicknesses [9, 10]. Therefore, a default encapsulation thickness of 20 μm was chosen for subsequent simulations.

Since impedance was largely unaffected by encapsulation thickness, a sensitivity analysis of encapsulation resistivity was performed in the model. With a default encapsulation thickness and interface resistivity of 20 μm and $1.8 \times 10^5 \Omega \text{ cm}$, respectively, the default encapsulation resistivity would have to increase by 17.8x to reach the mean impedance at week 12, as shown in figure 5. Therefore, the model was unable to adequately match the observed changes in impedance when it only considered the glial scar. This resulted in focus shifting to the interface between the recording site and surrounding neural tissue. The resistivity of the interface layer can be affected by many different factors such as biofouling [29, 30] and metallization loss [25].

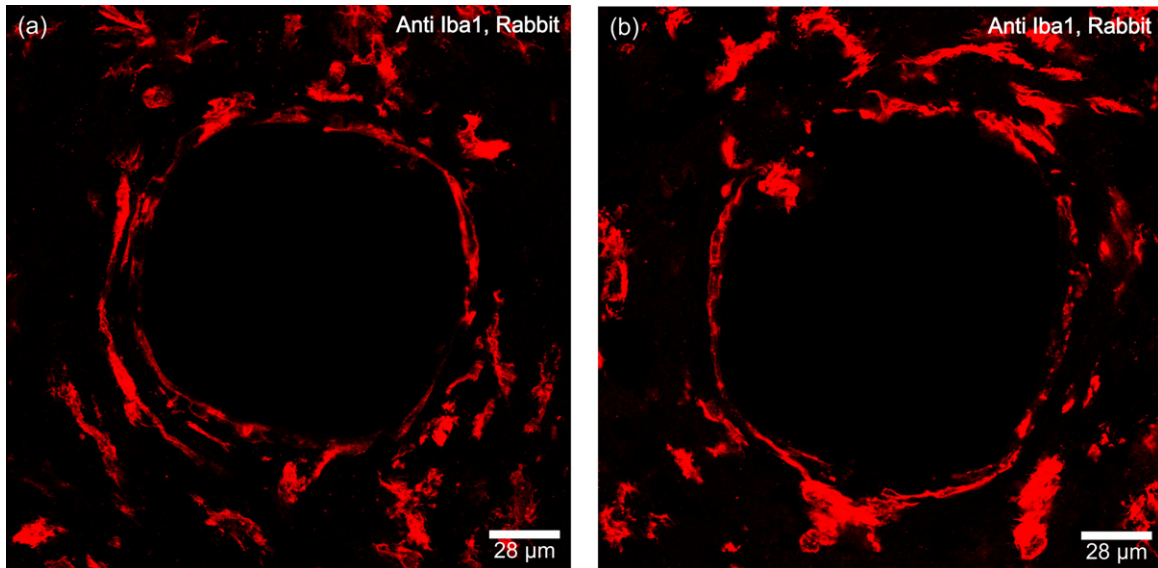


Figure 4. Gliosis around the electrodes obtained from one monkey seventeen weeks post-implantation. (a), (b) Tissue sections were taken from one array along the shanks. Microglia are stained red with Anti Iba1, Rabbit.

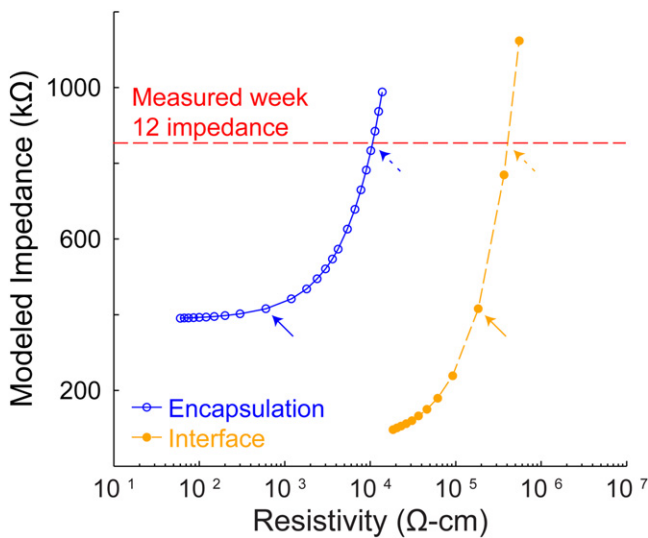


Figure 5. Effect of encapsulation and interface resistivity on impedance. Solid arrows denote the default encapsulation ($600 \Omega\text{-cm}$) and interface ($1.8 \times 10^5 \Omega\text{-cm}$) resistivity. Dashed arrows denote the encapsulation ($1.1 \times 10^4 \Omega\text{-cm}$) and interface ($4.1 \times 10^5 \Omega\text{-cm}$) resistivity necessary to match the measured mean impedance at week 12.

Therefore, a sensitivity analysis of interface resistivity was performed in the model. With a default encapsulation thickness and resistivity of $20 \mu\text{m}$ and $600 \Omega\text{-cm}$, respectively, the default interface resistivity would have to increase by only 2.2x to reach the mean impedance at week 12 (figure 5). Therefore, the model was better able to match the observed changes in impedance when it considered the thin interface around the electrode tip. Such a layer is meant to be representative of biofouling or metallization loss. However, the model does not differentiate between these two conditions.

Consistent with the population data, impedance trends for individual electrodes tended to increase during the first three

weeks post-implantation, showing considerable variation, and leveled out beyond week 3. Figures 6(a) and (b) show regression slope for all viable electrodes from three arrays at week 1–3 and 3–12, and table 2 summarizes the distributions (mean \pm standard deviation). Similar distributions were observed for the top twenty electrodes. Individual electrodes had significant ($p < 0.05$) positive and negative trends for week 3–12, although most were negative. A bootstrap analysis also yielded similar distributions, although week 1–3 showed more variation. Surprisingly, individual electrodes also had large and transient impedance differences from week-to-week in the positive and negative directions. Figure 6(c) shows week-to-week difference for all viable electrodes from three arrays at week 1–12. The distribution had a mean and standard deviation of 21.9 and 394.6 k Ω , respectively. Again, a similar distribution was observed for the top twenty electrodes ($n = 660$, $20.6 \pm 364.2 \text{ k}\Omega$). A small amount of this variability comes from the measurement system (figure 6(c)). Therefore, to test the accuracy of the Cerebus system, repeated impedance measurements were taken after removing and reattaching the connector between measurements, and without removing the connector between measurements (figure 6(c)). Measurement-to-measurement difference showed considerably less variation than week-to-week difference for removal/reattachment ($n = 504$, $1.0 \pm 143.5 \text{ k}\Omega$) and without removal ($n = 752$, $-1.9 \pm 17.3 \text{ k}\Omega$). The week-to-week difference in impedance from higher-impedance electrodes measured with an Autolab in another study that we performed in a rodent model was also examined [46]. Surprisingly, the differences showed even more variation ($n = 480$, $6.7 \pm 1.1 \times 10^3 \text{ k}\Omega$) compared to those observed in this study. While the computational model is able to capture a large range of impedances (figure 5), there currently is no aspect of the model that can explain the large week-to-week differences in impedance observed for the individual electrodes. The source of this impedance

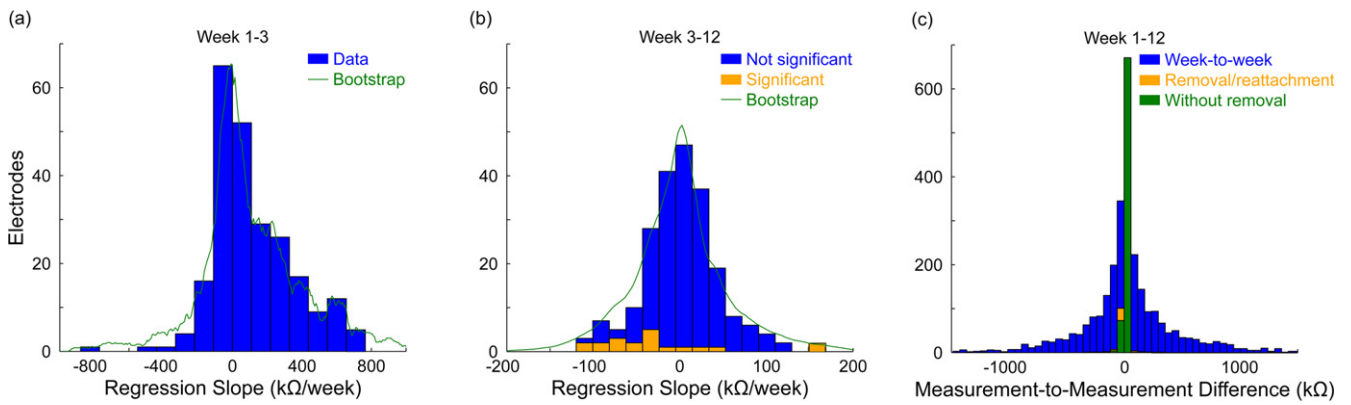


Figure 6. Distribution of regression slope and measurement-to-measurement difference in impedance (all viable electrodes (238/288)). (a) Week 1–3. (b) Week 3–12. (c) Week 1–12.

Table 2. Distribution of regression slope in impedance (kΩ/week).

All viable electrodes		Top twenty electrodes		Bootstrap	
Week 1–3	Week 3–12	Week 1–3	Week 3–12	Week 1–3	Week 3–12
115.8 ± 239.3	−0.7 ± 47.4	99.9 ± 226.1	4.2 ± 44.6	116.4 ± 332.9	−1.1 ± 58.5

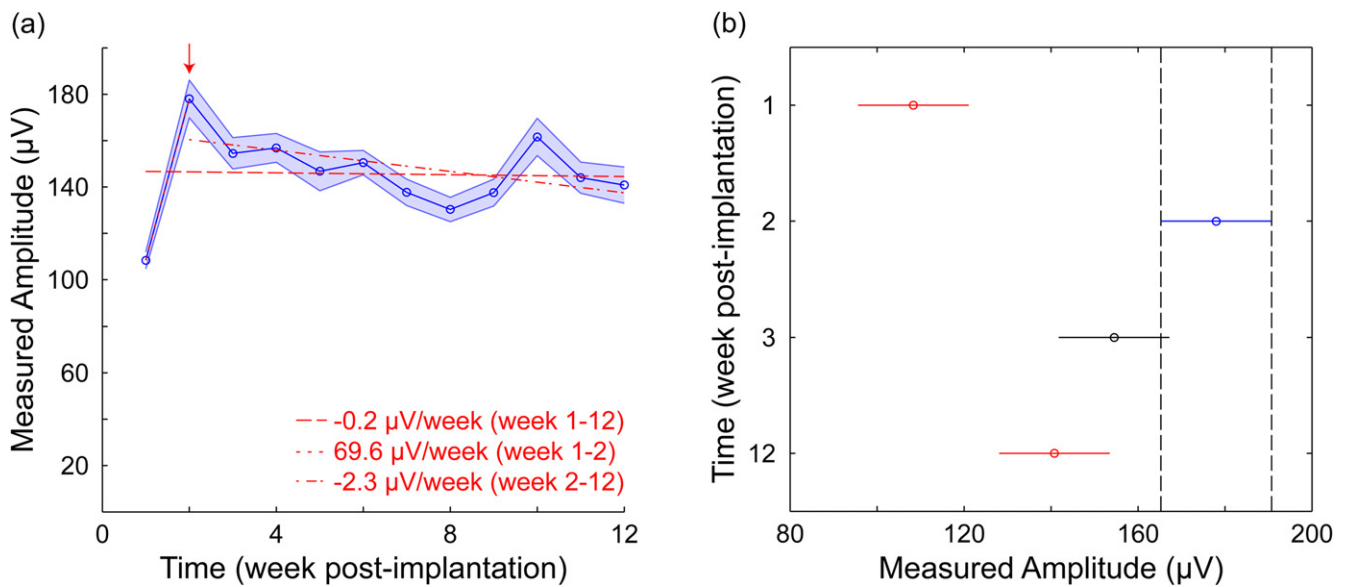


Figure 7. Mean amplitude over time (pooled arrays (3/4), all viable electrodes). (a) Week 1–12. Red lines are the linear regression fits. Arrow denotes week 2. Error bars denote the standard error of the mean. (b) Week 1, 2, 3, and 12. Bars denote the comparison intervals. Colour denotes the test group (blue) and significantly different groups (red).

variability remains to be identified. However, it may be difficult to pinpoint due to the dynamic nature of the neural environment.

3.2. Waveform amplitude

The amplitude of the action potential, rather than the impedance of the electrode, is the most important measure for assessing signal quality. Therefore, in addition to impedance, electrode stability was characterized by the peak-to-peak amplitude of the largest single-unit on each electrode. As an electrode is encapsulated by reactive tissue over time, it is

hypothesized that impedance increases and amplitude decreases [12–15]. However, multiple studies have reported being able to acquire neural signals over extended periods of time after scar formation [7, 18–22]. Therefore, amplitude was examined over the first twelve weeks post-implantation to determine if it was stable. Amplitude measurements were collected from the four arrays. As previously stated, one array was later excluded since it pulled out of the brain. However, its individual analyses are included in the supplementary data. Figure 7(a) shows mean amplitude (145.6 µV overall) for all viable electrodes from three arrays ($n = 238$). An overall linear decrease of $-0.2 \mu\text{V}/\text{week}$ was observed, but it was

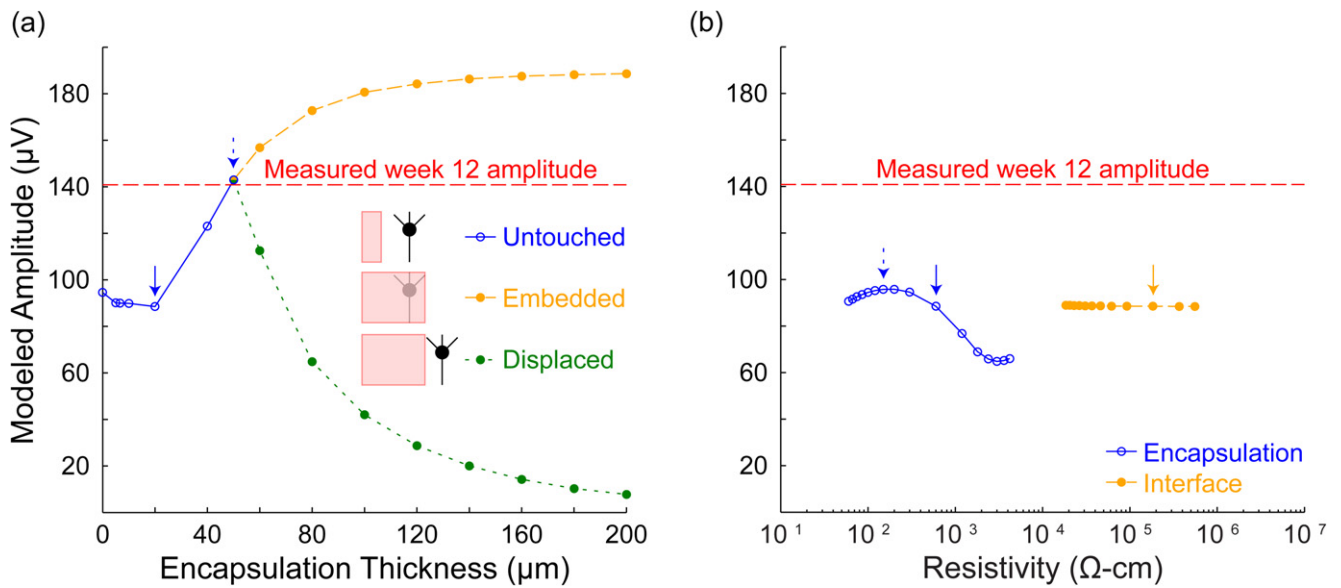


Figure 8. Effect of encapsulation and interface on amplitude. (a) Encapsulation thickness. In the untouched condition, the scar (red) does not contact the neuron (black) as it thickens (i.e., encapsulation thickness < 50 µm). In the embedded condition, the scar contacts and encapsulates the neuron (fixed in space) as it thickens beyond 50 µm. In the displaced condition, the scar contacts and moves the neuron (unfixed in space) as it thickens beyond 50 µm. Solid arrow denotes the default encapsulation thickness (20 µm). Dashed arrow denotes the default soma position (50 µm) relative to the electrode tip. (b) Encapsulation and interface resistivity. Simulation results are for the untouched condition in (a) (encapsulation thickness = 20 µm). Solid arrows denote the default encapsulation (600 Ω cm) and interface (1.8 × 10⁵ Ω cm) resistivity. Dashed arrow denotes the default encapsulation resistivity (150 Ω cm) for acute edema.

not significant ($p = 0.90$) at the 0.05 level. Amplitude (191.7 µV overall) was also examined for the top twenty electrodes with the largest single-units from three arrays ($n = 60$). An overall linear increase of 2.2 µV/week was observed, but it also was not significant ($p = 0.36$) at the 0.05 level. Furthermore, the amplitude trends had small regression slopes compared to impedance.

Like impedance, the initial ramp in amplitude during the first two weeks post-implantation [69.6 µV/week (all viable), 99.8 µV/week (top twenty)] stands out and is nominally consistent with a more resistive medium developing around the electrodes due to edema clearing as the injury stabilizes [33]. However, the time points do not match since amplitude increases from week 1–2 and impedance increases from week 1–3, similar to another study that we performed in a rodent model. Beyond week 2, the trend leveled out [–2.3 µV/week ($p = 0.07$, all viable), –1.2 µV/week ($p = 0.42$, top twenty)]. Figure 7(b) shows mean amplitude at week 1, 2, 3, and 12. Week 2 was significantly different from week 1 and 12 ($p < 0.001$, multiple comparisons). However, there was no significant difference between week 2 and week 3 ($p > 0.05$, multiple comparisons).

To determine if this weak amplitude trend was consistent with the computational model, a sensitivity analysis of encapsulation thickness, encapsulation resistivity, and interface resistivity was performed. With a default encapsulation and interface resistivity of 600 and 1.8 × 10⁵ Ω cm, respectively, encapsulation thickness had a small effect on amplitude for thin ($t < 20$ µm) scars not touching the neuron, as shown in figure 8(a) (untouched). For example, a 2x increase (10 to 20 µm) in encapsulation thickness resulted in a mere

1.6% decrease (–1.4 µV) in amplitude. Therefore, the model is consistent with the *in vivo* data. Between 20 and 50 µm, amplitude increased as encapsulation thickness increased (figure 8(a), untouched). Theoretically, if the neuron was to become embedded in the glial scar as it grew beyond 50 µm, then amplitude would continue increasing, eventually leveling out around 180 µV (figure 8(a), embedded). This makes sense, per Ohm’s law ($V = IR$), since the neuron now resides in a more resistive medium. However, if the scar was to displace the neuron as it grew beyond 50 µm, then amplitude would start decreasing (figure 8(a), displaced). For example, a 4x increase (20 to 80 µm, 30 µm displacement) in encapsulation thickness resulted in a 26.8% decrease (–23.7 µV) in amplitude. This suggests that neuron displacement has more of a negative effect on waveform amplitude than the electrical properties of the glial scar and offers a possible explanation of how amplitude may increase despite scarring, as observed in the neural data.

With a default encapsulation thickness, interface resistivity, and soma position of 20 µm, 1.8 × 10⁵ Ω cm, and 50 µm away from the bottom of the electrode tip, respectively, encapsulation resistivity had a moderate effect on amplitude, as shown in figure 8(b). For example, a 2x increase (600 to 1200 Ω cm) in encapsulation resistivity resulted in a 13.2% decrease (–11.7 µV) in amplitude. Furthermore, a 4x decrease (600 to 150 Ω cm, acute edema) resulted in an 8.2% increase (+7.3 µV). The increase in amplitude due to acute edema appears to contradict the increase observed during the first two weeks post-implantation that was attributed to a more resistive medium developing around the electrodes due to edema clearing as the injury

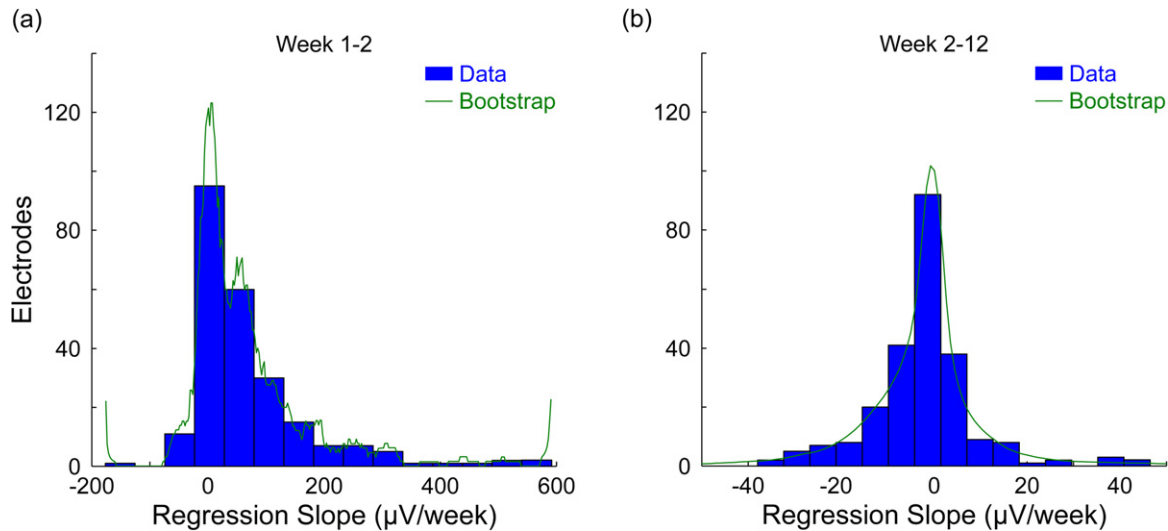


Figure 9. Distribution of regression slope in amplitude (all viable electrodes (238/288)). (a) Week 1–2. (b) Week 2–12.

Table 3. Distribution of regression slope in amplitude ($\mu\text{V}/\text{week}$).

All viable electrodes		Top twenty electrodes		Bootstrap	
Week 1–2	Week 2–12	Week 1–2	Week 2–12	Week 1–2	Week 2–12
69.6 ± 108.4	-2.3 ± 11.3	100.0 ± 150.6	-1.2 ± 18.2	70.0 ± 108.4	-2.2 ± 14.0

stabilizes. However, this assumes that the neuron is untouched (figure 8(a)) by the edematous encapsulation layer. It is more likely that the neuron becomes embedded in an edematous encapsulation upon electrode insertion, which later clears out. Alternatively, the neuron could be displaced by edema at first and then, as the swelling subsides, be moved closer to the recording site.

Interestingly, with a default encapsulation thickness, encapsulation resistivity, and soma position of $20\ \mu\text{m}$, $600\ \Omega\ \text{cm}$, and $50\ \mu\text{m}$ away from the bottom of the electrode tip, respectively, interface resistivity had a small effect on amplitude (figure 8(b)), consistent with previous studies [47, 48]. For example, a 6x increase (1.8×10^5 to $1.1 \times 10^6\ \Omega\ \text{cm}$) in interface resistivity resulted in a mere 0.1% decrease ($-0.1\ \mu\text{V}$) in amplitude. Despite impedance increasing by a few hundreds of kilohms due to increasing interface resistivity, the same recording characteristic was observed. As previously stated, interface resistivity was better able to match the changes in impedance, and it did so while maintaining signal stability. Therefore, this aspect of the model is consistent with the *in vivo* data. However, each of these model predictions require validation by future experiments.

Consistent with the population data, amplitude trends for individual electrodes tended to increase during the first two weeks post-implantation, showing less variation than those of impedance, and leveled out beyond week 2. Figure 9 shows regression slope for all viable electrodes from three arrays at week 1–2 and 2–12, and table 3 summarizes the distributions (mean \pm standard deviation). Similar distributions were observed for the top twenty electrodes. Individual electrodes

had positive and negative trends. None were significant. A bootstrap analysis also yielded similar distributions. Individual electrodes also had smaller amplitude differences from week-to-week in the positive and negative directions compared to those of impedance. The distribution of week-to-week difference for all viable electrodes from three arrays at week 1–12 had a mean and standard deviation of 2.9 and $105.6\ \mu\text{V}$, respectively. Again, a similar distribution was observed for the top twenty electrodes ($n = 660$, $7.2 \pm 165.8\ \mu\text{V}$).

3.3. Relationship between impedance and signal quality

Electrode impedance is often used as a predictor of signal quality. However, the computational model predicted interface resistivity to have a large effect on impedance and a small effect on amplitude. To determine if there was a relationship between impedance and amplitude in the *in vivo* data, amplitude was plotted as a function of impedance for all viable electrodes from three arrays ($n = 238$) at week 1–3 and 3–12, as shown in figures 10(a) and (b). There was a small, positive correlation for week 1–3 [$r = 0.06$ ($p = 0.10$)] and 3–12 [$r = 0.03$ ($p = 0.17$)], suggesting that increases in impedance result in increases in amplitude. However, the correlation was not significant for either period. This weak relationship between impedance and amplitude is consistent with the model predictions regarding interface resistivity.

To determine if changes in impedance corresponded to similar changes in amplitude, week-to-week difference in amplitude was plotted as a function of week-to-week difference in impedance, as shown in figures 10(c) and (d). There

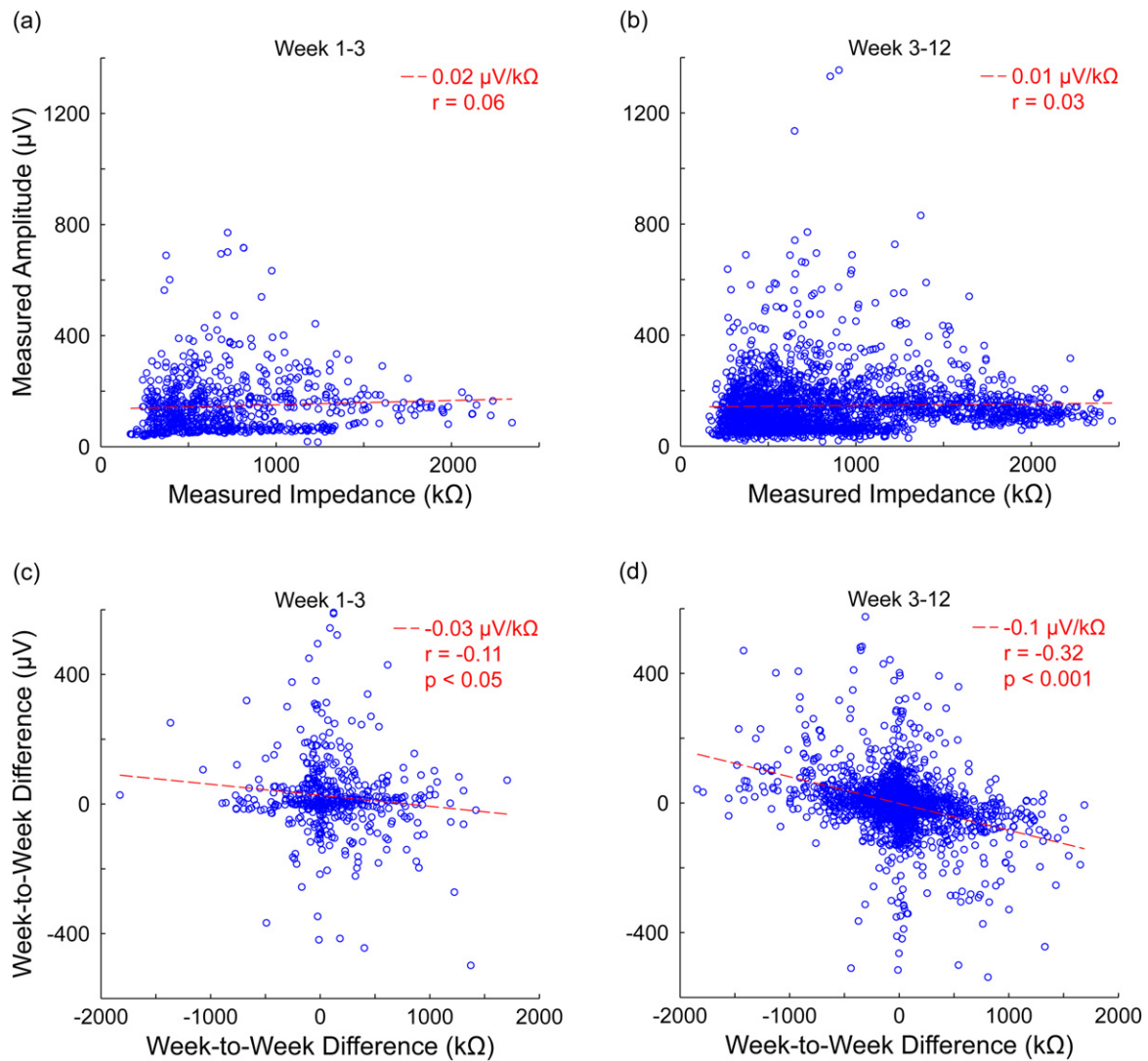


Figure 10. Correlation between impedance and amplitude (all viable electrodes (238/288)). (a), (b) Measured amplitude versus impedance (week 1–3, 3–12). Line is the linear regression fit. (c), (d) Week-to-week difference in amplitude versus week-to-week difference in impedance (week 1–3, 3–12). 9 data points were clipped from plot (d).

was a significant, negative correlation for week 1–3 [$r = -0.11$ ($p = 0.01$)] and 3–12 [$r = -0.32$ ($p = 2.59 \times 10^{-51}$)], suggesting that increases in impedance result in decreases in amplitude. However, the correlation was small despite its significance for both periods. This reversal in the relationship between impedance and amplitude suggests that impedance is not the best predictor of signal quality, especially since it can be manipulated independently [49].

Increasing noise due to increasing impedance could lead to difficulty detecting action potentials even in the absence of changes in waveform amplitude. Therefore, rms noise and SNR were examined over the first twelve weeks post-implantation to determine their trends. Rms noise and SNR measurements were collected from the four arrays. As previously stated, one array was later excluded since it pulled out of the brain. However, its individual analyses are included in the supplementary data. For the top twenty electrodes with the largest single-units from three arrays ($n = 60$), an overall linear increase of $0.4 \mu\text{V}/\text{week}$ and decrease of -2.2×10^{-4}

/week was observed for mean rms noise and SNR, respectively, but neither was significant ($p = 0.39$ and 0.997 , respectively) at the 0.05 level. The rms noise and SNR trends had small regression slopes. Therefore, signal quality was deemed stable despite increasing impedance over time, suggesting that noise was more biological than thermal.

4. Discussion

Past literature highlights glial scarring as one of the main factors affecting signal quality [8–17]. The scar is hypothesized to act as a high-impedance layer that electrically isolates the electrode from nearby neurons in the surrounding tissue [12, 13, 16, 17]. Because of this, electrode impedance is often used as a predictor of signal quality. Previous studies have reported direct correlations between scarring, impedance, and signal quality [12, 13, 16, 17]. However, others have reported the opposite, stating that no apparent correlation exists

between impedance and signal quality [7, 18, 26]. Previous studies have also reported being able to acquire neural signals over extended periods of time after scar formation [7, 18–22]. In this study, we show that the glial scar cannot adequately match *in vivo* impedance and neural recording data from chronically-implanted Utah arrays in rhesus macaques using a data-driven neural recording model. We then show how the interface between the recording site and surrounding neural tissue can better match the *in vivo* data.

Increases in electrode impedance and waveform amplitude were steep during the first three weeks post-implantation. Specifically, mean impedance and amplitude increased at a rate of 115.8 k Ω /week (figure 2(a)) and 23.1 μ V/week (figure 7(a)), respectively. This initial ramp in impedance and amplitude was observed across all four arrays (supplementary data), and is nominally consistent with proteins adhering to the recording site (increasing interface resistivity) and edema clearing as the injury stabilizes (increasing tissue resistivity around the electrode and neuron), respectively, in the computational model. Figure 7(a) shows that the time points do not match since waveform amplitude mainly ramps up from week 1–2, which is consistent with there being two separate processes that affect impedance and amplitude. A similar result was observed in another study that we performed in a rodent model [46].

In the model, the interface layer was better able to match the observed changes in impedance than the glial scar (figure 5). A possible explanation for this is that the interface is likely much more resistive than the encapsulation layer. Therefore, scarring does not appear to be the main contributor to increasing impedance, assuming that the encapsulation layer is not dramatically more resistive than the surrounding neural tissue. Based off experimental measurements, this assumption appears to be valid [43, 44]. Furthermore, there is no significant difference in impedance between simulations with and without a scar (figure 3).

The increase in amplitude observed during the first two weeks post-implantation (figure 7(a)) is nominally consistent with the development of a more resistive medium around the electrode and neuron in the model (figure 8(a), embedded), which can be attributed to edema clearing as the injury stabilizes [33]. However, glial scarring can decrease amplitude by moving neurons away from the recording site (figure 8(a), displaced) [14, 15]. Beyond week 2, amplitude decreased at a rate of -2.3 μ V/week for a loss of 37.2 μ V over the following ten weeks. This decrease is consistent with neuron displacement due to scarring, assuming a constant rate of scar growth. For example, a 10 μ m displacement in the model resulted in a 21.2% decrease (-30.4 μ V) in amplitude, which is consistent with the neural data. Despite the negative trend, amplitude at week 12 was not significantly different from week 3 ($p > 0.05$, multiple comparisons) (figure 7(b)). By combining the electrophysiological and histological (figure 4) data, it can be concluded that the tissue responses were not severe enough to isolate the electrodes from nearby neurons. Therefore, scarring does not appear to significantly affect amplitude once the scar has stabilized.

While interface resistivity had a large effect on impedance, the model did not predict it to have a large effect on amplitude (figure 8(b)). For example, a 6x increase (1.8×10^5 to 1.1×10^6 Ω cm) in interface resistivity resulted in a mere 0.1% decrease (-0.1 μ V) in amplitude. A possible explanation for this is that a thin interface at the recording site does not increase the resistivity of the medium that the neurons reside in, unlike glial scarring around the electrode. This is consistent with the standard assumption that the effect of the double layer at the interface on voltage measurements is negligible [47, 48]. However, this model prediction requires validation by future experiments.

Computational models are useful for performing analyses that would be difficult to implement experimentally. Since they cannot completely capture experimental conditions, assumptions have to be made when developing them and limitations have to be considered when interpreting their results. In this study, first, the brain and interface layer were assumed to be purely resistive and linear with regard to neural recordings [50]. Potential limitations with electrostatic solutions could be addressed by frequency-dependent models coupled with electrode impedance spectroscopy measurements that account for both the resistive and capacitive properties of the interface layer and neural tissue [51]. Second, the glial scar and interface layer were modeled as individual layers of uniform thickness in the FEM. This is a large simplification since, in reality, the scar and interface consist of cells around and proteins adhered to the electrode, respectively. This limitation could be addressed by incorporating more detailed and realistic encapsulation and interface layers into the model. Third, compartments of the neuron model within the encapsulation layer (6/531 compartments within the default 20 μ m thick scar) were kept in all simulations [33]. The physiological accuracy of this remains uncertain. However, this was done to maintain consistency between the embedded and untouched/displaced conditions examined in figure 8(a). Fourth, while the model is able to capture a large range of impedances (figure 5), there currently is no aspect of it that can explain the large week-to-week differences in impedance observed for individual electrodes (figure 6(c)). These differences are likely not a product of biofouling or metallization loss, which are relatively linear processes. This suggests that there is another factor crucial to the dynamics of the electrode–tissue interface and impedance measurements *in vivo* that remains to be revealed. However, it may be difficult to pinpoint due to the dynamic nature of the neural environment.

Another limitation of this study is that only a single antibody (Anti Iba1, Rabbit) was used to estimate encapsulation thickness (figure 4). Iba1 is specifically expressed in resident microglia and non-resident macrophages. However, the fibrous encapsulation layer around the electrodes is mostly comprised of reactive astrocytes, which usually form a thicker and more robust encapsulation than microglia [15]. While it is possible that the encapsulation thickness reported in this study is underestimated, the estimate was found to be comparable to other observed encapsulation thicknesses [9, 10]. Furthermore, a range of encapsulation thicknesses (0–200 μ m) were

examined in the model with regard to impedance and amplitude, so thicker scars were accounted for. This limitation could be addressed by using additional stains (e.g., glial fibrillary acidic protein (GFAP), vimentin) and obtaining histology from more than one animal and one array.

5. Conclusion

Overall, the results of this study challenge current hypotheses regarding the glial scar and its effect on chronic neural recordings by suggesting that the scar does not cause an electrical problem with regard to signal quality. In the computational model, molecular elements (e.g., proteins) that adhere to the surface of the recording site (i.e., biofouling) are treated distinctly from cellular elements (e.g., microglia, astrocytes) that encapsulate the electrode (i.e., scarring). By doing so, we were able to identify interesting observations regarding the implication of the interface layer and electrode impedance. While this layer could increase impedance by hundreds of kilohms in the model, the lack of correlation between interface resistivity and waveform amplitude suggests a divergence between the effect of scarring on impedance and amplitude, which may help to explain the lack of correlation between impedance and amplitude observed by others [7, 18, 26]. Furthermore, glial scarring does not appear to insulate the electrodes from neural signals [12, 13, 16, 17], as has been commonly thought. Rather, neuron displacement due to scar growth may be a more likely explanation for signal loss at the electrode–tissue interface over time [14, 15]. Previous studies have shown that it is possible to record action potentials over extended periods of time after scar formation [7, 18–22]. This suggests that neural signals can be obtained reliably despite scarring as long as the recording site has sufficiently low impedance after accumulating a thin layer of biofouling. Since the scar may only need a few months to stabilize, material failures may be more of a concern when dealing with longer time scales [7, 23–25]. Therefore, advancements in microelectrode technology may be expedited by focusing on improvements to the interface between the recording site and surrounding neural tissue (e.g., reduction of biofouling, preservation of metallization) rather than elimination of the glial scar.

Acknowledgments

The authors would like to thank K Bennett for expert veterinary care. This material is based upon work supported by a National Science Foundation Graduate Research Fellowship (KAM), Ford Foundation Predoctoral Fellowship (KAM), and Rackham Merit Fellowship (KAM).

References

- [1] Taylor D M, Tillery S I and Schwartz A B 2002 Direct cortical control of 3D neuroprosthetic devices *Science* **296** 1829–32
- [2] Hochberg L R, Serruya M D, Friehs G M, Mukand J A, Saleh M, Caplan A H, Branner A, Chen D, Penn R D and Donoghue J P 2006 Neuronal ensemble control of prosthetic devices by a human with tetraplegia *Nature* **442** 164–71
- [3] Collinger J L *et al* 2014 Collaborative approach in the development of high-performance brain–computer interfaces for a neuroprosthetic arm: translation from animal models to human control *Clin. Transl. Sci.* **7** 52–9
- [4] Williams J C, Rennaker R L and Kipke D R 1999 Long-term neural recording characteristics of wire microelectrode arrays implanted in cerebral cortex *Brain Res. Brain Res. Protocol* **4** 303–13
- [5] Vetter R J, Williams J C, Hetke J F, Nunamaker E A and Kipke D R 2004 Chronic neural recording using silicon-substrate microelectrode arrays implanted in cerebral cortex *IEEE Trans. Biomed. Eng.* **51** 896–904
- [6] Nordhausen C T, Maynard E M and Normann R A 1996 Single unit recording capabilities of a 100 microelectrode array *Brain Res.* **726** 129–40
- [7] Barrese J C, Rao N, Paroo K, Triebwasser C, Vargas-Irwin C, Franquemont L and Donoghue J P 2013 Failure mode analysis of silicon-based intracortical microelectrode arrays in non-human primates *J. Neural Eng.* **10** 066014
- [8] Stensaas S S and Stensaas L J 1976 The reaction of the cerebral cortex to chronically implanted plastic needles *Acta Neuropathol.* **35** 187–203
- [9] Turner J N, Shain W, Szarowski D H, Andersen M, Martins S, Isaacson M and Craighead H 1999 Cerebral astrocyte response to micromachined silicon implants *Exp. Neurol.* **156** 33–49
- [10] Szarowski D H, Andersen M D, Retterer S, Spence A J, Isaacson M, Craighead H G, Turner J N and Shain W 2003 Brain responses to micro-machined silicon devices *Brain Res.* **983** 23–35
- [11] Polikov V S, Tresco P A and Reichert W M 2005 Response of brain tissue to chronically implanted neural electrodes *J. Neurosci. Methods* **148** 1–18
- [12] Johnson M D, Otto K J and Kipke D R 2005 Repeated voltage biasing improves unit recordings by reducing resistive tissue impedances *IEEE Trans. Neural Syst. Rehabil. Eng.* **13** 160–5
- [13] Otto K J, Johnson M D and Kipke D R 2006 Voltage pulses change neural interface properties and improve unit recordings with chronically implanted microelectrodes *IEEE Trans. Biomed. Eng.* **53** 333–40
- [14] Edell D J, Toi V V, McNeil V M and Clark L D 1992 Factors influencing the biocompatibility of insertable silicon microshafts in cerebral cortex *IEEE Trans. Biomed. Eng.* **39** 635–43
- [15] Biran R, Martin D C and Tresco P A 2005 Neuronal cell loss accompanies the brain tissue response to chronically implanted silicon microelectrode arrays *Exp. Neurol.* **195** 115–26
- [16] Williams J C, Hippensteel J A, Dilgen J, Shain W and Kipke D R 2007 Complex impedance spectroscopy for monitoring tissue responses to inserted neural implants *J. Neural Eng.* **4** 410–23
- [17] Prasad A and Sanchez J C 2012 Quantifying long-term microelectrode array functionality using chronic *in vivo* impedance testing *J. Neural Eng.* **9** 026028
- [18] Suner S, Fellows M R, Vargas-Irwin C, Nakata G K and Donoghue J P 2005 Reliability of signals from a chronically implanted, silicon-based electrode array in non-human

- primate primary motor cortex *IEEE Trans. Neural Syst. Rehabil. Eng.* **13** 524–41
- [19] Fraser G W, Chase S M, Whitford A and Schwartz A B 2009 Control of a brain–computer interface without spike sorting *J. Neural Eng.* **6** 055004
- [20] Kruger J, Caruana F, Volta R D and Rizzolatti G 2010 Seven years of recording from monkey cortex with a chronically implanted multiple microelectrode *Front. Neuroeng.* **3** 6
- [21] Chestek C A et al 2011 Long-term stability of neural prosthetic control signals from silicon cortical arrays in rhesus macaque motor cortex *J. Neural Eng.* **8** 045005
- [22] Simeral J D, Kim S P, Black M J, Donoghue J P and Hochberg L R 2011 Neural control of cursor trajectory and click by a human with tetraplegia 1000 days after implant of an intracortical microelectrode array *J. Neural Eng.* **8** 025027
- [23] Prasad A, Xue Q-S S, Dieme R, Sankar V, Mayrand R C, Nishida T, Streit W J and Sanchez J C 2014 Abiotic–biotic characterization of Pt/Ir microelectrode arrays in chronic implants *Front. Neuroeng.* **7** 2
- [24] Takmakov P, Ruda K, Scott Phillips K, Isayeva I S, Krauthamer V and Welle C G 2015 Rapid evaluation of the durability of cortical neural implants using accelerated aging with reactive oxygen species *J. Neural Eng.* **12** 026003
- [25] Xie X, Rieth L, Williams L, Negi S, Bhandari R, Caldwell R, Sharma R, Tathireddy P and Solzbacher F 2014 Long-term reliability of Al₂O₃ and Parylene C bilayer encapsulated Utah electrode array based neural interfaces for chronic implantation *J. Neural Eng.* **11** 026016
- [26] Cui X, Wiler J, Dzaman M, Altschuler R A and Martin D C 2003 *In vivo* studies of polypyrrole/peptide coated neural probes *Biomaterials* **24** 777–87
- [27] Selvakumaran J, Keddie J L, Ewins D J and Hughes M P 2008 Protein adsorption on materials for recording sites on implantable microelectrodes *J. Mater. Sci. Mater. Med.* **19** 143–51
- [28] Green R A, Hassarati R T, Bouchinet L, Lee C S, Cheong G L, Yu J F, Dodds C W, Suaning G J, Poole-Warren L A and Lovell N H 2012 Substrate dependent stability of conducting polymer coatings on medical electrodes *Biomaterials* **33** 5875–86
- [29] Sommakia S, Rickus J L and Otto K J 2009 Effects of adsorbed proteins, an antifouling agent and long-duration DC voltage pulses on the impedance of silicon-based neural microelectrodes *Conf. Proc. IEEE Eng. Med. Biol. Soc.* **2009** 7139–42
- [30] Sommakia S, Gaire J, Rickus J L and Otto K J 2014 Resistive and reactive changes to the impedance of intracortical microelectrodes can be mitigated with polyethylene glycol under acute *in vitro* and *in vivo* settings *Front. Neuroeng.* **7** 33
- [31] Mainen Z F, Joerges J, Huguenard J R and Sejnowski T J 1995 A model of spike initiation in neocortical pyramidal neurons *Neuron* **15** 1427–39
- [32] Holt G R and Koch C 1999 Electrical interactions via the extracellular potential near cell bodies *J. Comput. Neurosci.* **6** 169–84
- [33] Moffitt M A and McIntyre C C 2005 Model-based analysis of cortical recording with silicon microelectrodes *Clin. Neurophysiol.* **116** 2240–50
- [34] Lempka S F, Johnson M D, Moffitt M A, Otto K J, Kipke D R and McIntyre C C 2011 Theoretical analysis of intracortical microelectrode recordings *J. Neural Eng.* **8** 045006
- [35] Reimann M W, Anastassiou C A, Perin R, Hill S L, Markram H and Koch C 2013 A biophysically detailed model of neocortical local field potentials predicts the critical role of active membrane currents *Neuron* **79** 375–90
- [36] Henze D A, Borhegyi Z, Csicsvari J, Mamiya A, Harris K D and Buzsaki G 2000 Intracellular features predicted by extracellular recordings in the hippocampus *in vivo* *J. Neurophysiol.* **84** 390–400
- [37] Hatsopoulos N, Joshi J and O’Leary J G 2004 Decoding continuous and discrete motor behaviors using motor and premotor cortical ensembles *J. Neurophysiol.* **92** 1165–74
- [38] Thelin J, Jörntell H, Psouni E, Garwicz M, Schouenborg J, Danielsen N and Linsmeier C E 2011 Implant size and fixation mode strongly influence tissue reactions in the CNS *PLoS One* **6** e16267
- [39] Logothetis N K, Kayser C and Oeltermann A 2007 *In vivo* measurement of cortical impedance spectrum in monkeys: implications for signal propagation *Neuron* **55** 809–23
- [40] McIntyre C C and Grill W M 2001 Finite element analysis of the current–density and electric field generated by metal microelectrodes *Ann. Biomed. Eng.* **29** 227–35
- [41] Cantrell D R, Inayat S, Taflove A, Ruoff R S and Troy J B 2008 Incorporation of the electrode–electrolyte interface into finite-element models of metal microelectrodes *J. Neural Eng.* **5** 54–67
- [42] Høyum P, Kalvøy H, Martinsen Ø G G and Grimnes S 2010 A finite element model of needle electrode spatial sensitivity *Physiol. Meas.* **31** 1369–79
- [43] Grill W M and Mortimer J T 1994 Electrical properties of implant encapsulation tissue *Ann. Biomed. Eng.* **22** 23–33
- [44] Haeuelsen J, Tuch D S, Ramon C, Schimpf P H, Wedeen V J, George J S and Belliveau J W 2002 The influence of brain tissue anisotropy on human EEG and MEG *Neuroimage* **15** 159–66
- [45] Carnevale N T and Hines M L 2006 *The NEURON Book* (New York: Cambridge University Press)
- [46] Patel P R, Zhang H, Robbins M T, Nofar J B, Marshall S P, Kobylarek M J, Kozai T D Y, Kotov N A, Kipke D R and Chestek C A 2015 Carbon fiber microelectrode arrays for neuroprosthetic and neuroscience applications *PhD Thesis* University of Michigan
- [47] Moulin C, Glière A, Barbier D, Joucla S, Yvert B, Mailley P and Guillemaud R 2008 A new 3D finite-element model based on thin-film approximation for microelectrode array recording of extracellular action potential *IEEE Trans. Biomed. Eng.* **55** 683–92
- [48] Nelson M J, Pouget P, Nilsen E A, Patten C D and Schall J D 2008 Review of signal distortion through metal microelectrode recording circuits and filters *J. Neurosci. Methods* **169** 141–57
- [49] Purcell E K, Thompson D E, Ludwig K A and Kipke D R 2009 Flavopiridol reduces the impedance of neural prostheses *in vivo* without affecting recording quality *J. Neurosci. Methods* **183** 149–57
- [50] Bédard C, Kröger H and Destexhe A 2004 Modeling extracellular field potentials and the frequency-filtering properties of extracellular space *Biophys. J.* **86** 1829–42
- [51] Lempka S F and McIntyre C C 2013 Theoretical analysis of the local field potential in deep brain stimulation applications *PLoS One* **8** e59839